Influence of build characteristics and chamber oxygen concentration on powder degradation in laser powder bed fusion

Timothée Delacroix[a,*], Fernando Lomello[a], Frédéric Schuster[b], Hicham Maskrot[a], Christina Baslari[a], Ulysse Gaumet[a], Yanis Flici[b], Jean-Paul Garandet[c]

[a] Université Paris-Saclay, CEA, Service d'Études Analytiques et de Réactivité des Surfaces, 91191, Gif-sur-Yvette, France
[b] Université Paris-Saclay, CEA, Cross-Cutting Program on Materials and Processes Skills, 91191 Gif-sur-Yvette, France
[c] Université Grenoble Alpes, CEA, LITEN, DTNM, F-38000 Grenoble, France

[*] **Corresponding author:** Timothée Delacroix – timothee.delacroix@outlook.fr

DOI : 10.1016/j.powtec.2023.118231

Abstract

Powder reuse is essential in laser powder bed fusion (L-PBF) to limit material waste and improve the process sustainability. However, complex laser-material interactions result in an inevitable alteration of the attributes of the recovered powder at the end of the fabrications. Powder degradation is influenced by numerous factors including the processing parameters but also the build topology. In this work, various build characteristics were studied to develop a better understanding of the effects on powder degradation, with the aim of minimizing it. L-PBF prints with different melted volume fractions, part spacings and fabrication heights were conducted using stainless steel 316L (SS316L) material. Powders recovered on the build platform, as well as in zones of interest directly adjacent to solidified areas were characterized to investigate the changes in particles characteristics, with special regards to powder oxidation. In combination with these geometrical features, the effect of the oxygen concentration in the build chamber was also studied. The results allow to identify the relation between the oxygen content of recovered powder and the volume fraction of printed parts. It also highlights the presence of heat-affected zones in the near vicinity of the parts with a strong oxygen pick-up in a 500 µm wide zone around the consolidated material. The results also show the significance of the oxygen concentration in the process atmosphere, with a less severe oxidation and fewer ejecta in the powder recovered after printing under 300 wppm O_2 compared to 1000 wppm O_2.

Keywords: Laser Powder Bed Fusion, Powder characterization, Chamber atmosphere, Build topology, Stainless steel

1. Introduction

Laser powder bed fusion (L-PBF) is one of the most mature metal additive manufacturing (AM) technology and is already used industrially in several sectors such as aerospace, healthcare, automotive or energy [1,2]. This success is attributed to the almost unlimited design possibilities offered by the process, combined with resulting excellent mechanical properties of the printed parts [3,4]. However, costs remain too high for markets with high-volume productions, due to relatively small build volumes, quite slow build rates, and high powder material costs [5–7]. During the process, only a small fraction of the powder bed is generally consolidated as parts. Powder reuse after each printing (also sometimes referred to somewhat improperly as powder recycling) is thus essential for the process sustainability and reliability. A number of recycling studies have been detailed in the literature, dealing with various materials such as titanium alloys [8–11], aluminum alloys [11–13], nickel alloys [11,14–16] or stainless steels [17–22]. All these studies showed that the powder recovered at the end of a manufacturing cycle is inevitably degraded, and the phenomena are amplified by repeated powder reuse. The most significant and recurring alteration of powder attributes concerns its oxygen concentration, which gradually increases with powder recycling. This can result in various consequences for the printed parts properties, such as a density decrease, an increase of their oxygen content as well, or even an alteration of the mechanical properties [8,9,20,21,23].

The alteration of recovered powder is globally related to the exposition to a high temperature environment during the L-PBF process, due to different phenomena occurring in connection to the interaction between the laser beam and the material. First, during laser scanning and powder melting, considerable amounts of material ejection are observed, commonly referred to as spatters, which are dispersed and can fall back on the powder bed area. Major efforts have been made to study and understand the mechanisms of spatter generation in L-PBF, e.g. by means of coupled in-situ imaging and modelling [24–29]. Spatter can be ejected directly from the melt pool, driven by recoil pressure associated to the evaporation of some alloying elements. In addition, Marangoni convection due to surface tension variations in the melt pool can also lead to liquid flow instabilities and ejecta. A second mechanism of spattering has been demonstrated by Matthews et al. [30] and Ly et al. [31], namely the entrainment of powder particles in proximity of the melt pool by the metal vapor flow, creating local denudation zones [32,33]. The vapor-entrained particles can be subcategorized into hot spatters and cold spatters, depending on whether the particles are carried into or near the laser beam and heated, or whether they travel without passing through the beam [31]. The chamber atmosphere is filled with a protective gas such as argon or nitrogen, however significant amounts of residual oxygen remain, that allow spatter particles oxidation at the high temperatures encountered during the process. Numerous factors also directly affect the generation and oxidation of spatters in L-PBF, such as the laser beam power, diameter and scanning speed, the type of material, or the build chamber environment and protective gas [27,34–37]. For example, it was observed by Taheri et al. [38] that a decrease of the laser power or an increase of the scanning speed can reduce spatter formation. However, in any case, spatter generation cannot be totally avoided, and adequate processing conditions to produce dense materials are needed. As such, an insufficient input energy even though it may be favorable from the spatters standpoint, can not be accepted as it leads to defects such as lack-of-fusion pores. The characteristics of spatter particles have been widely explored, and the latter generally feature a selective oxidation on their surface, with the presence of oxide nodules composed of elements with great affinity to oxygen [39–43]. The residual oxygen concentration in the build chamber can influence the severity of oxidation of spatters. Raza et al. [44] found that reducing the oxygen concentration during the L-PBF process enables to lower the oxygen content found in Inconel718 hot spatters.

In addition to the degradation of recovered powder due to spatters contamination, a second group of altered particles can be distinguished, consisting of unmelted particles present in the Heat-Affected Zones (HAZ) in the vicinity of the solidified parts [17,21]. These particles are close enough to the heat source and can therefore be subjected to modifications, with cycling heating of the parts with successive laser scanning. The severity of particles oxidation in the HAZ is mainly influenced by the type of alloy, the residual oxygen concentration in the build chamber and the laser scanning speed, resulting in various oxide thicknesses and observable particles of different colors [21].

A schematization of the L-PBF process, with illustrations of the main phenomena occurring during laser-material interaction is shown in Fig. 1. The two categories of altered particles (spatters and particles in the HAZ), as well as the two subcategories of spatters (melt pool spatters and vapor-entrained particles) are indicated in the side view schematic.

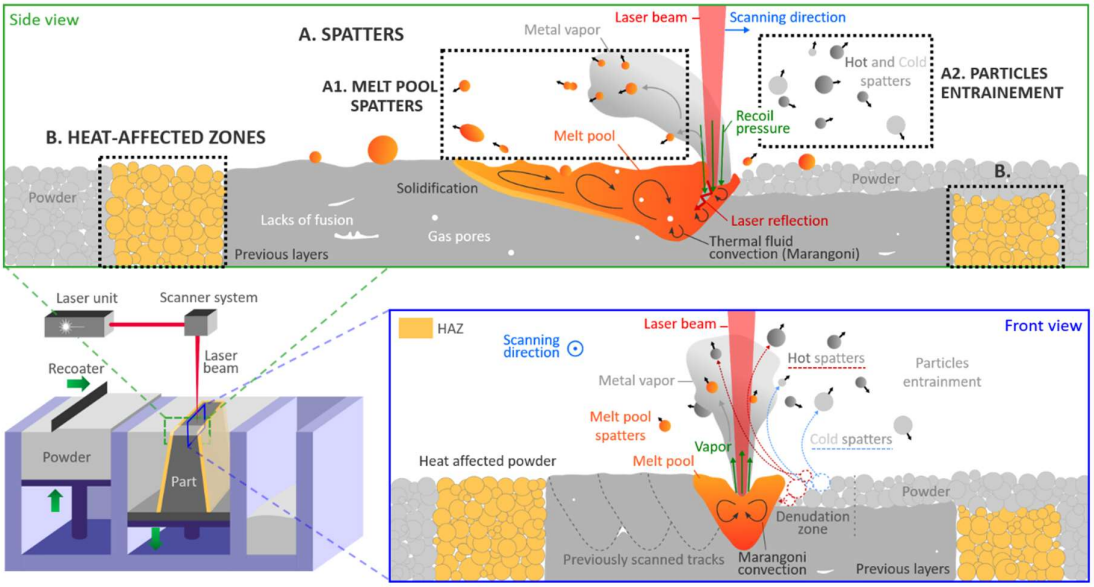

Fig. 1. Schematic illustration of laser-material interactions in L-PBF process showing the different categories of altered particles found in recycled powders (adapted from [31] and [45]).

It thus appears that in all cases, powder oxidation depends on the environment conditions, *i.e.* temperature, exposure time and atmosphere composition and that the topology of the build (printed parts volume fraction and positioning) will inevitably affect the quantity of altered material [46]. Indeed, the parts geometrical characteristics can make a significant difference in the reusability of the powder and need to be further explored [46]. For instance, the melted volume is related to the amount of material exposed to the laser beam and thus to the associated by-products and heat affected zones. Components nesting during L-PBF, with part spacing often minimized for optimum build volume utilization, are parameters that will also influence powder degradation. The existing recycling studies did focus on overall powder degradation, but mostly with fixed processing conditions and build geometries. A better understanding of the influence of build characteristics and processing parameters on powder degradation would allow to strongly minimize its alteration and thus to improve the sustainability of powder reuse.

To bring further insights in the mechanisms and the influential factors leading to powder degradation [12], the present work has for objective to assess the effects of build topology and chamber oxygen content on the degradation of recovered powder in L-PBF. To the authors knowledge, only a few studies focused on the effects of the printed parts geometries [47,48]. Kriewall et al. [47] studied

different area fraction and part spacing and found changes in terms of particle size distribution, phase fraction and amount of powder sieved off, but did not investigate the oxygen contents. Galicki et al. [48] found that the oxygen content in recovered powder was dependent of the relative position to the melt zones. More precisely, our objective is thus to study the effect of parts volume fraction and spacing, fabrication height, *i.e.* the duration of the process, and of the chamber oxygen concentration on the recovered powder. For this purpose, numerous L-PBF fabrications are conducted using standard stainless steel 316L material (SS316L) and manufacturing parts of various volumes, spacings and heights. In addition, all fabrications are produced twice, with a fairly high but commonly used residual oxygen content of 1000 ppm (in weight) in the build chamber, and a more limited one of 300 ppm O_2. Powder recovered on the build platform after the prints, as well as in zones of interest directly adjacent to melt areas is characterized to investigate the changes in particles attributes, with special regards to powder oxidation.

2. Materials and methods

2.1. Material and L-PBF process

A gas-atomized AISI 316L powder supplied by Oerlikon Metco Europe GmbH was used in this study. Standard chemical composition of the powder, provided by the supplier and confirmed by chemical analyses using inductively coupled plasma atomic emission spectrometry, glow discharge mass spectrometry and inert gas fusion, is listed in Table 1. This commercial powder presents a particle size distribution in the range of 20 – 45 µm, with a rather spherical shape (see Fig. 2), that can be considered standard for L-PBF implementation.

Table 1. Chemical composition of the SS316L powder provided by Oerlikon Metco, in wt.%.

Element	Fe	Cr	Ni	Mn	Mo	Si	N	C	P	S	O
wt%	Bal.	17.5	12.6	1.5	2.4	0.04	0.07	0.02	0.002	0.001	0.048

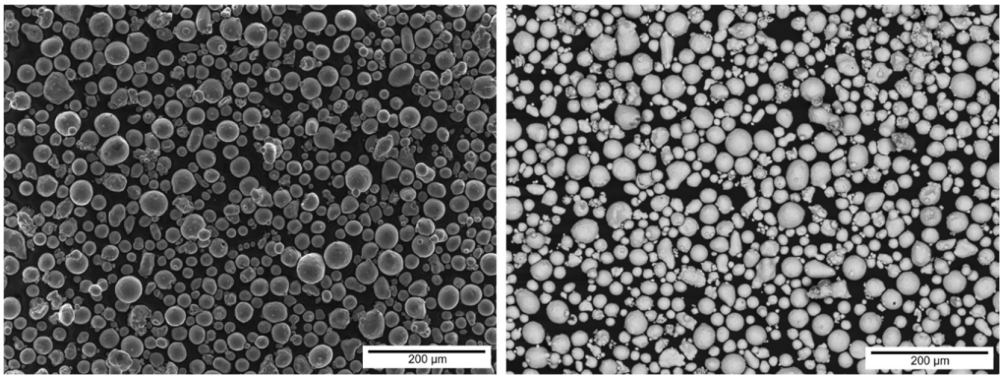

Fig. 2. SEM micrographs (SE and BSE images) of the virgin SS316L powder used in the present study.

Parts were produced by L-PBF with a TruPrint series 1000 machine from TRUMPF GmbH. The printer is equipped with a 1070 nm fiber laser with a maximal power of 200 W and a spot diameter of 55 µm. Optimized processing parameters leading to high-density specimens (> 99.9 %) were employed, with a laser power of 165 W, a scanning speed of 950 mm/s, a hatch distance of 50 µm and a layer thickness of 30 µm [21]. High-purity argon (Argon 5.7) shielding gas with a controlled laminar flow rate of 3 m/s over the build platform generates a protective atmosphere during fabrication. An

oxygen concentration limit is specified by the operator, with a strategy consisting in a reintroduction of inert gas to the system if the detected oxygen level exceeds the target.

2.2. Powder degradation study methodology

The different factors investigated in this study of powder degradation are schematized in Fig. 3. Four melted volume fractions were studied, with the elaboration of cubic specimens inside square walls, accounting for a volume (and surface) fraction of 10 %, 25 %, 50 % and 75%. The square walls were printed to facilitate volume calculations and especially the recovery of the powder in the area at the end of the fabrication. The influence of parts spacing and height was explored with the manufacturing of walls of fixed width (10 mm) separated by grooves of different spacing: S0.5, S1, S2, S3, S15 and S30, the values being expressed in mm. In addition, three different heights of 10 mm, 25 mm and 50 mm (referred to as H10, H25 and H50 in the following) were elaborated for each spacing. The powder within each groove was collected separately for local characterization. Finally, as mentioned in the introduction, two different oxygen concentrations inside the build chamber were tested for each condition previously described. The prints were carried out first with a maximum requirement for residual oxygen content of 300 ppm, and replicated with an O_2 target of 1000 ppm, all oxygen content values being expressed in weight.

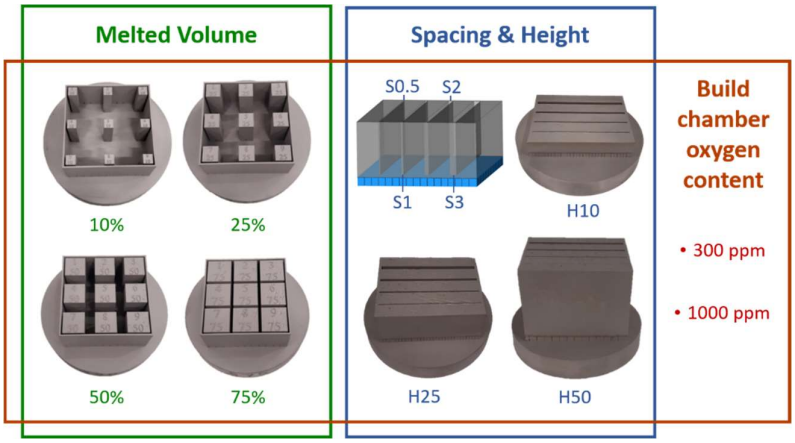

Fig. 3. Chart of the powder degradation study methodology.

2.3. Characterization methods

The powder samples recovered for each condition (inside the square walls for the melted volume study and inside each groove for the spacing and height study) were sieved using a 50 µm screen in a Retsch AS 300 vibratory sieving station. Powder oxygen content was measured by inert gas fusion, using an Horiba EMGA 820 AC analyzer. For each sample, three to five repeatability measurements were conducted. Particles color and morphology were observed by means of optical microscopy (OM) on a ZEISS Axio Imager 2 instrument, and scanning electron microscopy (SEM) on a JEOL JSM-7000 F with a field-emission gun. For a semi-quantitative evaluation of the surface composition of the particles, X-ray energy dispersive spectroscopy (EDS) was employed. As for phase identification, X-ray diffraction (XRD) analysis was carried out using a Bruker D8 Advance spectrometer with Cu Kα radiation source under 40kV voltage, 40 mA current, over an angular range of 40-120° with a 0.02° step size. Particle size distribution was determined by laser granulometry using a Horiba Partica LA-950 granulometer, with five measurements of at least 5000 particles per condition. In addition to

the characterization of the powder, a limited characterization of printed parts characterization has been performed, with the evaluation of the roughness of the elaborated surfaces according to different parts spacing and height. To this end, 3D optical profilometry was conducted, using a Bruker ContourGT-K optical profiler, with three area-based measurements per condition on 1255 µm x 941 µm surfaces.

3. Results and discussion

3.1. Effect of parts volume fraction and chamber oxygen concentration

The oxygen content of the recovered powder as a function of the melted volume fraction in the L-PBF print is displayed in Fig. 4. The two conditions of build chamber oxygen concentration are represented with the blue (300 ppm O_2) and red (1000 ppm O_2) series, the dotted lines indicating the linear trendlines of the two series are shown as guide to the eyes. Regardless of the oxygen concentration in the build chamber, the powder recovered at the end of the fabrication present a significantly higher oxygen content when a larger volume has been solidified as parts. A second observation is that for all conditions of parts volume fraction, recovered powder oxygen content is higher when the prints were conducted with a residual oxygen concentration of 1000 ppm in the process chamber, compared to those carried out with a maximum oxygen level of 300 ppm. As a reminder, the virgin powder presents an oxygen content value around 475 ppm.

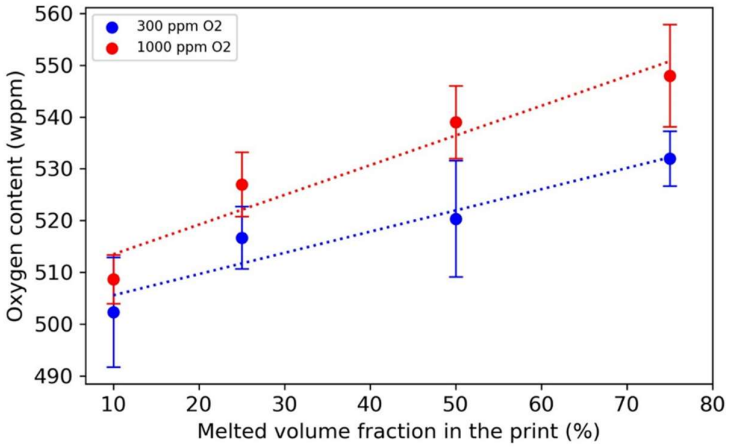

Fig. 4. Oxygen content of the recovered powder as a function of the melted volume fraction in the print and chamber oxygen concentration.

Observations by SEM reveal that greater amounts of oxidized particles with surface dark spots were found in the powder samples coming from the prints with 75% of melted volume (V75, see Fig. 5 (a)). EDS mapping in Fig. 5 (b) and point analysis shows that these dark spots are oxides nodules rich in Mn and Si on their surface, likely coming from the high-temperature oxidation of such spatter particles in L-PBF [21]. This oxide composition was found to be similar in all tested conditions. No differences appear observable on these images as a function of the oxygen concentration in the build chamber, nor on optical microscopy observations. However, the latter showed an increase of the number of uniformly colored particles with increased melted volume fraction. These observations are not unexpected with this change in parts geometry. Indeed, an increase in part volume results in

longer laser scan distances and, consequently, a greater amount of material ejection. In addition, the perimeters of the parts are also longer, leading to larger HAZ.

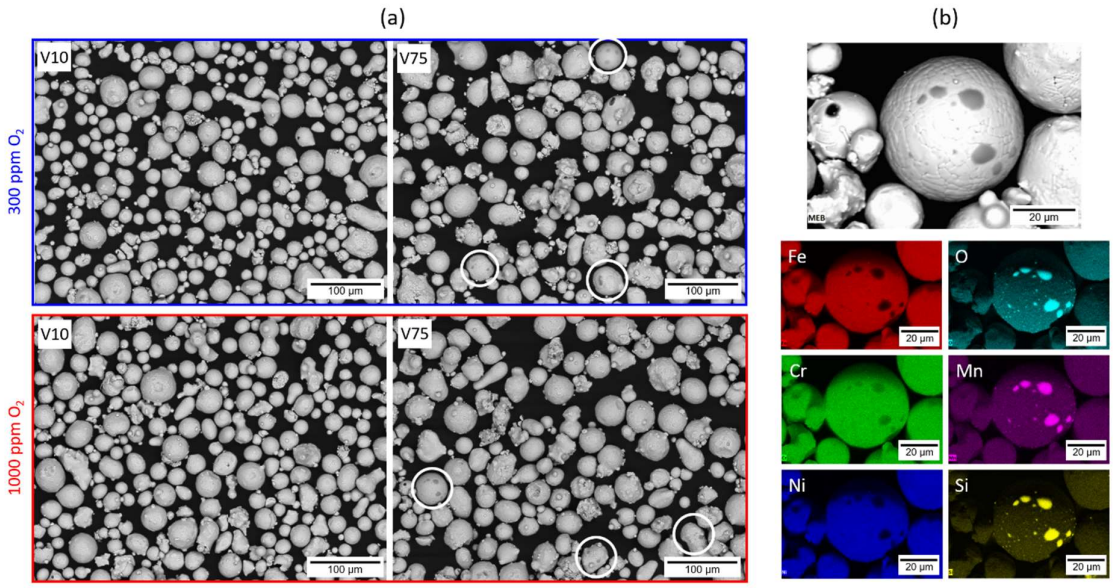

Fig. 5. (a) BSE micrographs of V10 and V75 powders from fabrications with a chamber oxygen concentration of 300 ppm and 1000 ppm. White circles highlight particles with surface oxide nodules. (b) EDS maps of a partially oxidized particle with selective surface oxidation.

Sieved residues (SR) were analyzed to obtain more information about this oxygen difference in the recovered powders from different conditions of processing chamber atmosphere. Fig. 6 presents the mass fraction of powder discarded by the sieving step compared to the total amount of powder recovered at the end of the L-PBF process, as a function of the part volume fraction in the print and the chamber oxygen level during the process. It can be seen that the higher the volume of material is consolidated as parts, the higher the mass fraction of large particles in the recovered powder. In addition, all the observed fractions of SR in the powder samples are more important for the prints conducted with the highest chamber oxygen concentration of 1000 ppm. This shows that for any print job in L-PBF, more agglomerates and large particles are produced if the oxygen level target in the build chamber is higher. The same phenomenon was observed in the literature for titanium [49] and nickel alloys [40]. Oxygen is known to influence the process, the morphology of the tracks, the surface tension of the melt pool, and the spattering effect [35,50–52].

Fig. 7 shows SEM images of the SR of V10 powders from L-PBF processing with chamber oxygen levels of 300 ppm (in blue) and 1000 ppm (in red). It is noticeable that a more severe oxidation is present for the 1000 ppm sample. Oxide nodules are more numerous and more coalesced, covering larger surfaces on the particles. This observation is confirmed by oxygen contents measurements, with global values of 1325 and 1072 wppm for the chamber atmosphere conditions of respectively 1000 ppm and 300 ppm of residual oxygen.

It can be expected that the observed phenomena also occur for smaller spatter particles that pass through the sieving mesh. Among those, hot spatters, that are known to be found in the higher amounts [31], could also be presenting larger and most numerous oxide nodules. A more severe oxidation might also apply to particles in the HAZ subjected to solid-state oxidation. This, combined with a greater number of ejecta generated under a higher partial pressure of oxygen in the L-PBF

system, allows to qualitatively explain the differences in recovered powder oxygen content measured by inert gas fusion.

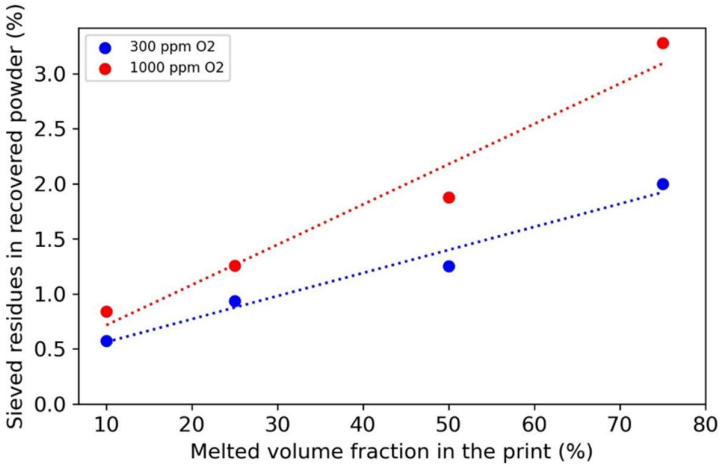

Fig. 6. Fraction of sieved residues in the recovered powder (wt.%) as a function of the melted volume fraction in the print and chamber oxygen concentration.

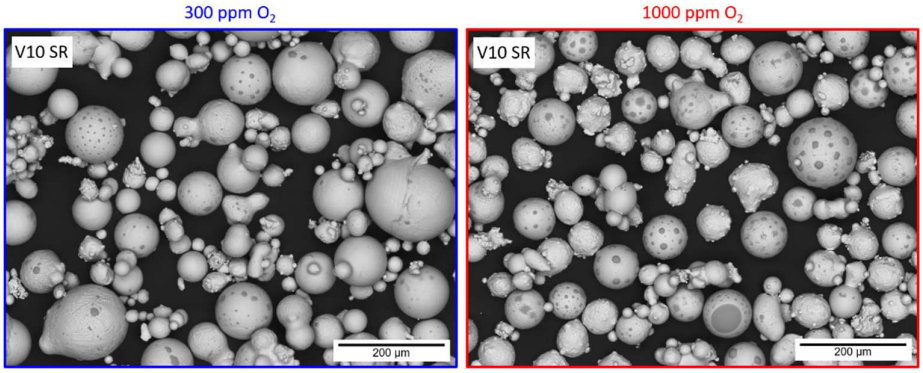

Fig. 7. BSE micrographs of sieved residues of V10 powders (V10 SR) form the prints conducted with a chamber oxygen concentration of 300 ppm and 1000 ppm.

The SEM micrographs presented in Fig. 5 provides information about the presence of partially oxidized particles, but also on the particles size. In these images, it appears that the particles tend to be smaller and more numerous for both conditions of V10 samples, compared to the V75 powders. Laser granulometry was performed on all 8 sieved samples to assess the potential size changes in the powders recovered at the end of the prints with various parts volume fractions. The obtained particle size distributions (PSD) characteristics values of D_{10}, D_{50} and D_{90} are displayed in Fig. 8. Although size variations between all conditions are minor, trends can nevertheless be observed. Slight increases of the characteristic size values are found when the melted volume in the build is more important, with more significant variations for the D_{90} values especially. The values of the 1000 ppm oxygen series are marginally higher than those of the 300 ppm series. Let us recall that the previous results showed that more sieved residues and spatters were observed for larger fractions of consolidated material, and for the prints conducted with the highest chamber oxygen concentration. Even though the large ejecta are discarded by the sieving, some can be smaller than the mesh size but still larger the virgin powder, or can be larger but elongated allowing them if they are favorably oriented to pass through.

Vapor-entrained particles can also be exposed to the laser beam totally or partially and merge with each other, or small particles can attach to spatters as satellites, which increases the particle size. An additional factor could be the really large ejecta that fall down on powder bed areas in semi-liquid state creating large agglomerates with the sintering of small 'as-virgin' particles, which are then removed by the sieve, thus reducing the number of fine particles and shifting the PSD towards larger values. It is likely that the observations of these size trends after one powder recovery would be accentuated by successive reuse of the powder in L-PBF.

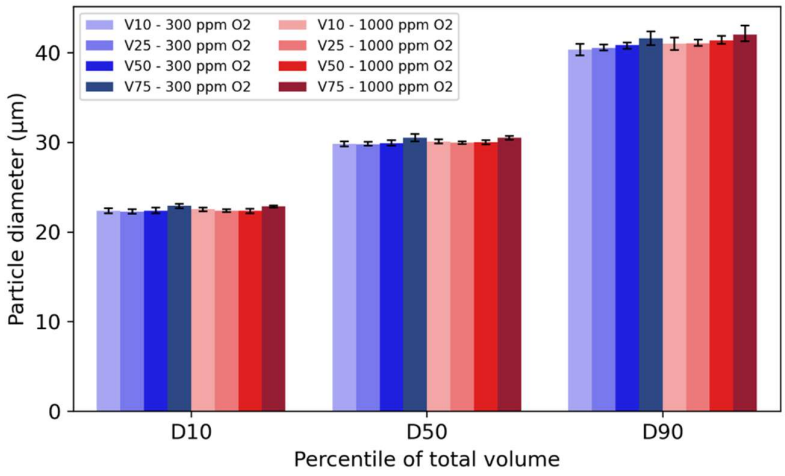

Fig. 8. Particle size distributions D_{10}, D_{50}, and D_{90} of the recovered powders collected from L-PBF prints of different melted volume fractions and conducted with 300 ppm and 100 ppm of oxygen in the build chamber.

XRD was performed on all samples to investigate the crystal structure of the recovered powders. No differences were found in the diffractograms with respect to either the different part volumes or the chamber oxygen concentrations. Only austenitic peaks are present, with no discernible δ-ferrite peak allowing a Rietveld refinement for phase proportions calculation. This result is not in line with our previous work on the topic, where ferritic fractions up to 4 wt.% had been observed. However, in this previous work, those 4% were observed after 15 reuse cycles, so it is likely that after only one cycle ferrite would not be present in amounts detectable by DRX. The absence of ferrite is also a priori not consistent with the results of Kriewall et al. [47], who found an increase in ferritic particles with larger melted volumes of stainless steel 304L and over three iterations of recycling. However, in their study, XRD analysis was carried out before powder sieving. This could explain the difference compared to the present results. Magnetic particles were still identified in the different powder samples, but were mostly found in abundance in the sieved residues due to their magnetic attraction.

3.2. Effect of part spacing, height and chamber oxygen concentration

Unmelted powder collected inside each groove of different spacing between consolidated walls was sieved and analyzed in terms of oxygen content. The obtained results are shown in Fig. 9 as a function of the six different space distances between solidified parts, with three different part heights. The blue data points correspond to powders recovered from L-PBF prints carried out with 300 ppm of residual oxygen in the processing chamber, and the red data points represent powders

recovered after processing performed with 1000 ppm of oxygen. The oxygen content of the powder is seen to increase when the part spacing is reduced. It must be noted that the x-axis shows the different spacings as categories and not in a linear format. Therefore, the increase of oxygen is actually very progressive until a 1 mm spacing, then quite abrupt with a spacing reduction to 500 µm. The pickup is about the same amount between 1 and 0.5 mm of part spacing than between 30 mm and 1 mm, around 30 wppm. This shows that powder oxidation is strongly related to the particles oxidized in the HAZ close to the printed parts, and not only by spatter particles. Another important observation is that a 30 mm spacing between printed parts greatly limits powder degradation, with oxygen content values relatively close to the one of the virgin powder (474 wppm), when the oxygen concentration in the chamber during manufacturing is 300 ppm. The recovered powders oxygen contents are systematically higher after build jobs conducted with 1000 ppm of oxygen in the chamber. As for the melted volume study in the previous section, a higher oxygen partial pressure during L-PBF might promote the oxidation of particles at high temperatures, with thicker oxide layer or larger oxide nodules, resulting in higher overall oxygen contents. Regarding the influence of parts height, it can be observed that fore large spacings (S15 and S30), higher parts lead to higher oxygen contents. This effect is still relatively present for distances of 3 mm and 2 mm between consolidated parts. For even smaller spacings, parts height no longer has any impact, with the oxygen pickup being governed by such narrow spacings and reaching a plateau. Parts height is directly related to build time. As an indication, fabrications with 10 mm, 25 mm and 50 mm high parts (supports not included) lasted 10 h, 23 h and 43 h respectively (supports included). A longer printing time results in a longer exposition of a number of particles to high temperatures. Indeed, it has been shown by Yavari et al. [53] that the surface temperature of the parts gradually increases through the superposition of scanned layers in the L-PBF process. The longer times at high temperatures, combined with gradually higher temperatures during the process with repeated laser scanning must have led to thicker oxide layer growths and thus higher overall measured oxygen contents.

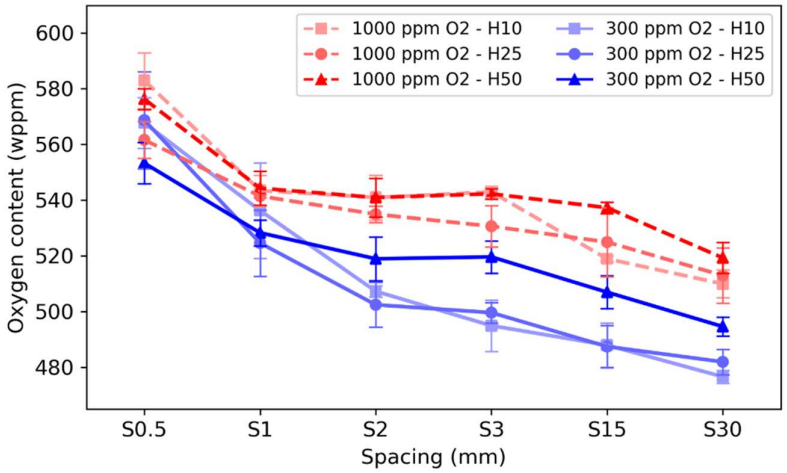

Fig. 9. Oxygen content of the recovered powder as a function of the parts spacing, fabrication height and chamber oxygen concentration.

Optical microscopy was carried out to analyze the colors of the particles in the different grooves. The influence of part spacing is highlighted in Fig. 10, with S0.5, S1, S3 and S30 powder samples with the two conditions of chamber oxygen level. Numerous colored particles are noticeable for the smallest spacing, with yellow/orange, purple and blue particles. An increase of the spacing leads to a smaller

number of colored particles among the recovered powder. Oxidation seems more pronounced for the 1000 ppm O_2 series in terms of both the number of colored particles but also the shade of the colors. Increased oxidation of stainless steel leads to various colorings according to the following sequence: pale yellow, dark yellow, brown, purple brown, purple, blue, dark blue [54]. It appears that "lighter" colors are visible for the powders after processing under 300 ppm of oxygen. However, highly oxidized blue particles are still present for the samples with this condition. In any case, the samples did not show only one type of color in addition to the grey virgin particles, but almost all oxidation states. Observations for the different parts heights did not evidence significant change towards specific colors either, although as mentioned earlier build height variations result in longer or shorter exposure times to high temperature for the powders present in the HAZ. An increase of parts height from 10 mm to 25 mm and 50 mm shows a slight increase in the number of colored particles, which is in accordance with the measurements of oxygen content by inert gas fusion.

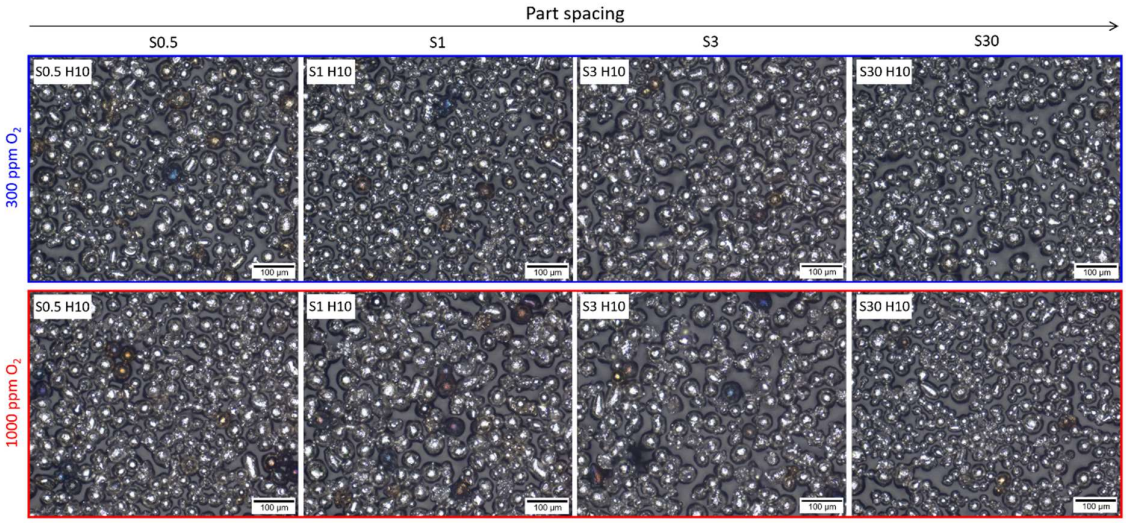

Fig. 10. Optical images of recovered powders from S0.5, S1, S3 and S30 spacings from fabrications of 10 mm high (H10), conducted with a chamber oxygen concentration of 300 ppm and 1000 ppm.

SEM observations were carried out as well on the powder samples. Surprisingly regarding the low probabilities of spatter fallout in the very small spacing grooves (S0.5, S1), the latter present a large number of ejecta compared to powders recovered in larger spacings (S3 and above). However, these observations do not allow to conclude about the distribution of the spatters redeposition, because of the various directions followed by the laser. Zigzag scanning, rotations between layers can lead to spatter ejection in about every direction. In addition, other factors such as the gas flow are known to influence spatter redeposit [55,56].

As for the analysis of the effects of melted volume fraction in section 3.1, XRD was conducted on the powder sample from the spacing experiments and did not show any significant difference in crystallographic phases. It is assumed that the magnetic particles are small spatter particles that were ejected from the melt pool at high speed, or vapor-entrained particles with high velocities leading to fast cooling rates and this resulting different solidification [18,21,42]. The small powder bed spacings do not have a high probability of ejecta fallout, and therefore of significant increase in ferritic content with this local characterization of powder samples in each groove.

Preliminary parts characterization was performed with measurements of average areal surface roughness Sa (in µm). Fig. 11 (a) presents the results of the analyses conducted on the side surfaces of 50 mm high parts printed with 1000 ppm of O_2, for four different spacings (S1, S3, S15 and S30). Three different height zones were evaluated per spacing, with height A located approximately 10 mm above the substrate, height B in the middle of the part around 25 mm high, and height C close to the top surface at about 45 mm high. It can be seen that the location measurement along the part height strongly influences the surface roughness. For each spacing, roughness values are gradually larger with increasing height. The mean Sa of zones A are the smaller ones, and the values are increased by 18 % in zone B, while zone C measurements are increased by 32 % in average compared to the values of zone A, that increase representing around 7 µm independently of spacing. In addition to fabrication height, part spacing has also a significant impact on absolute roughness values. The maximum roughness is observed for the smallest spacing tested (1 mm), and an increase of space distance reduces the roughness. As for the results of oxygen content as a function of the part spacing, the increase in surface roughness is again far from gradual when observed on a linear scale axis. The rise of Sa is rather progressive from 30 mm to 3 mm, with a gain of about 3 µm averaged over the three heights, then is quite abrupt with a similar increase with only a reduction of part spacing by 2 mm (to S1). Analysis of the local side surface relief maps of each condition was carried out. Fig. 11 (b) shows the outcomes for the S1 and S30 spacings and the three height zones. This reveals that the increase in roughness along the height is mainly due to the sintering of more particles and potentially larger ones to the side surface. It can be assumed that the overall increase of part temperature with repeated laser scanning allows the sintering of more numerous particles surrounding the part during melting and solidification. Spatter can also fall back in all conditions such as semi-liquid state, but also in a cold state [31] and sinter to the surface because of that part elevated temperature. At the beginning of the process where the heat sink effect of the substrate plate is expected to be stronger, relatively lower temperatures might not have provoked this sintering phenomenon.

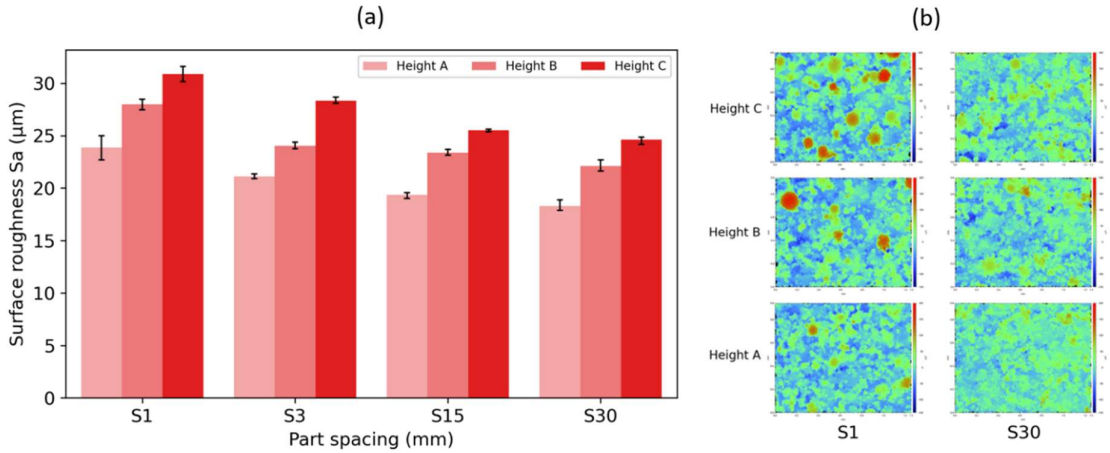

Fig. 11. (a) Roughness of the printed parts side surface as a function of part spacing and height; (b) Surface height maps of S1 and S30 side surfaces for the three height zones.

4. Conclusions

In this study, the effects of several L-PBF process and build parameters on powder degradation were evaluated, with the purpose of minimizing feedstock alteration during its reuse. Numerous prints

were conducted to investigate the impact of different melted volume fractions in the prints, part spacings, fabrication heights and build chamber oxygen concentration on the powder to be reused. The main findings are summarized as follows:

- The solidification of larger volumes as parts during L-PBF processing leads to an increase of the fraction of sieved material in relation to the total amount of recovered powder on the build platform at the end of the manufacturing.
- After sieving, the oxygen content of the recovered powder increases gradually with the melted volume fraction in the print. Slightly more numerous colored particles are observed with larger solidified areas, likely resulting from longer perimeters on the surface of each layer, *i.e.* larger heat-affected zones. More spatters with selective oxidation of Mn and Si are also present after sieving, because of the greater distances covered by the laser beam and complex interactions with the powder resulting in more material ejecta.
- Recovered powder shows a slight increase in particle size with larger consolidated volumes.
- A reduction of part spacing results in a local elevation of the oxygen content in recovered powders. A strong oxygen pickup, characterized by larger proportions of colored particles, is observed when the distance between parts is reduced to 500 µm. Conversely, a part spacing of 30 mm strongly limits powder degradation and oxidation, with powder oxygen content and attributes close to the ones of the virgin powder.
- Fabrication height has an impact on the recovered powder for large part spacings, with more color-oxidized particles and higher oxygen contents. Higher parts imply longer printing times, leading to an increase in part temperature with successive addition of layers and repeated laser scanning. For small spacings (0.5 - 1 mm), the effect of fabrication height is less important, reaching a plateau, likely because the powders oxygen intake is governed by such small part spacing distances.
- The build height also affects significantly the parts side surface roughness, which increases along the build direction, with more numerous and larger particles sintered during melting and solidification close to the surface. The roughness also increases with a reduction of part spacing.
- A higher oxygen concentration in the build chamber during L-PBF processing accentuates all the previously described phenomena. Processing with 1000 wppm of residual oxygen compared to 300 wppm leads to an increase of the amount of sieved residues, spatter particles in the sieved powders, colored particles, and overall oxygen contents in all comparable conditions.

It thus appears that powder degradation and mainly its oxidation is inevitable during the L-PBF process. However, some parameters and manufacturing characteristics allow to strongly limit the kinetics of alteration and favor an extended powder reuse. Part geometry, with smaller melted volumes associated with large enough space between parts can greatly contribute to minimize the effects. Moreover, the chamber oxygen concentration plays a crucial role, and its restriction to levels well below the 1000 ppm limit often found in industrial printers is necessary in view of the objective of repeated powder reuse.

Further investigation should be focused on this issue, as well as other factors of interests. The use of a heating plate during the manufacturing process, useful in particular to reduce the residual stresses of the parts, must certainly have a strong impact on the powders remaining on the powder bed. It would also be interesting to assess as well complex geometries such as lattice structures, which are of interest in AM. Such geometries present a high surface/volume ratio, therefore larger numbers of particles in heat affected zones that could lead to significantly different results as compared to those

obtained in the present study using geometrically simple parts. Magnetic sieving should be implemented to quantify changes in crystallographic phase fractions in the powder samples more efficiently. Additional parts characterization would also be interesting, such as the density and mechanical properties of elaborated specimens as a function of build topology and chamber oxygen content.

CRediT authorship contribution statement

Timothée Delacroix: Conceptualization, Methodology, Validation, Investigation, Writing - original draft, Writing - review & editing, Visualization. **Fernando Lomello:** Writing – review & editing, Supervision. **Frédéric Schuster:** Conceptualization, Funding acquisition. **Hicham Maskrot:** Resources, Project administration. **Christina Baslari:** Investigation, Validation. **Ulysse Gaumet:** Investigation, Validation. **Yanis Flici:** Investigation, Validation. **Jean-Paul Garandet:** Conceptualization, Writing – review & editing, Supervision.

Declaration of Competing Interest

The authors declare that they have no known competing financial interests or personal relationships that could have appeared to influence the work reported in this paper.

Acknowledgments

The authors gratefully acknowledge the technical and financial support provided by the CEA Cross-Cutting Program on Materials and Processes Skills, France.

References

[1] Wohlers Associates (Firm), T.T. Wohlers, I. Campbell, O. Diegel, R. Huff, J. Kowen, Wohlers Report 2022: 3D Printing and Additive Manufacturing Global State of the Industry, Wohlers Associates, 2022. https://books.google.fr/books?id=CyUGzwEACAAJ.

[2] W.E. Frazier, Metal Additive Manufacturing: A Review, J. Mater. Eng. Perform. 23 (2014) 1917–1928. https://doi.org/10.1007/s11665-014-0958-z.

[3] T. DebRoy, H.L. Wei, J.S. Zuback, T. Mukherjee, J.W. Elmer, J.O. Milewski, A.M. Beese, A. Wilson-Heid, A. De, W. Zhang, Additive manufacturing of metallic components – Process, structure and properties, Prog. Mater. Sci. 92 (2018) 112–224. https://doi.org/10.1016/j.pmatsci.2017.10.001.

[4] Y.M. Wang, T. Voisin, J.T. McKeown, J. Ye, N.P. Calta, Z. Li, Z. Zeng, Y. Zhang, W. Chen, T.T. Roehling, R.T. Ott, M.K. Santala, P.J. Depond, M.J. Matthews, A.V. Hamza, T. Zhu, Additively manufactured hierarchical stainless steels with high strength and ductility, Nat. Mater. 17 (2018) 63–71. https://doi.org/10.1038/nmat5021.

[5] A. Khorasani, I. Gibson, J.K. Veetil, A.H. Ghasemi, A review of technological improvements in laser-based powder bed fusion of metal printers, Int. J. Adv. Manuf. Technol. 108 (2020) 191–209. https://doi.org/10.1007/s00170-020-05361-3.

[6] M. Barclift, S. Joshi, T.W. Simpson, C.J. Dickman, Cost Modeling and Depreciation for Reused Powder Feedstocks in Powder Bed Fusion Additive Manufacturing, Proc. 27th Annu. Int. Solid Free. Fabr. Symp. SFF 2016. (2016) 2007–2028.
[7] M. Baumers, C. Tuck, R. Wildman, I. Ashcroft, E. Rosamond, R. Hague, Combined build-time, energy consumption and cost estimation for direct metal laser sintering, 23rd Annu. Int. Solid Free. Fabr. Symp. - Addit. Manuf. Conf. SFF 2012. (2012) 932–944.
[8] A. Strondl, O. Lyckfeldt, H. Brodin, U. Ackelid, Characterization and Control of Powder Properties for Additive Manufacturing, JOM. 67 (2015) 549–554. https://doi.org/10.1007/s11837-015-1304-0.
[9] P.E. Carrion, A. Soltani-Tehrani, N. Phan, N. Shamsaei, Powder Recycling Effects on the Tensile and Fatigue Behavior of Additively Manufactured Ti-6Al-4V Parts, JOM. 71 (2018) 963–973. https://doi.org/10.1007/s11837-018-3248-7.
[10] O.A. Quintana, J. Alvarez, R. Mcmillan, W. Tong, C. Tomonto, Effects of Reusing Ti-6Al-4V Powder in a Selective Laser Melting Additive System Operated in an Industrial Setting, JOM. 70 (2018) 1863–1869. https://doi.org/10.1007/s11837-018-3011-0.
[11] L. Cordova, M. Campos, T. Tinga, Revealing the Effects of Powder Reuse for Selective Laser Melting by Powder Characterization, JOM. 71 (2019) 1062–1072. https://doi.org/10.1007/s11837-018-3305-2.
[12] A. Raza, T. Fiegl, I. Hanif, A. MarkstrÖm, M. Franke, C. Körner, E. Hryha, Degradation of AlSi10Mg powder during laser based powder bed fusion processing, Mater. Des. 198 (2021) 109358. https://doi.org/10.1016/j.matdes.2020.109358.
[13] H. Asgari, C. Baxter, K. Hosseinkhani, M. Mohammadi, On microstructure and mechanical properties of additively manufactured AlSi10Mg_200C using recycled powder, Mater. Sci. Eng. A. 707 (2017) 148–158. https://doi.org/10.1016/j.msea.2017.09.041.
[14] L.C. Ardila, F. Garciandia, J.B. González-Díaz, P. Álvarez, A. Echeverria, M.M. Petite, R. Deffley, J. Ochoa, Effect of IN718 Recycled Powder Reuse on Properties of Parts Manufactured by Means of Selective Laser Melting, Phys. Procedia. 56 (2014) 99–107. https://doi.org/10.1016/j.phpro.2014.08.152.
[15] K. Gruber, I. Smolina, M. Kasprowicz, T. Kurzynowski, Evaluation of Inconel 718 Metallic Powder to Optimize the Reuse of Powder and to Improve the Performance and Sustainability of the Laser Powder Bed Fusion (LPBF) Process, Materials. 14 (2021) 1538. https://doi.org/10.3390/ma14061538.
[16] X. He, D. Kong, Y. Zhou, L. Wang, X. Ni, L. Zhang, W. Wu, R. Li, X. Li, C. Dong, Powder recycling effects on porosity development and mechanical properties of Hastelloy X alloy during laser powder bed fusion process, Addit. Manuf. 55 (2022) 102840. https://doi.org/10.1016/j.addma.2022.102840.
[17] F.C. Pinto, I.R. Souza Filho, M.J.R. Sandim, H.R.Z. Sandim, Defects in parts manufactured by selective laser melting caused by δ-ferrite in reused 316L steel powder feedstock, Addit. Manuf. 31 (2020) 100979. https://doi.org/10.1016/j.addma.2019.100979.
[18] M.J. Heiden, L.A. Deibler, J.M. Rodelas, J.R. Koepke, D.J. Tung, D.J. Saiz, B.H. Jared, Evolution of 316L stainless steel feedstock due to laser powder bed fusion process, Addit. Manuf. 25 (2019) 84–103. https://doi.org/10.1016/j.addma.2018.10.019.
[19] A.T. Sutton, C.S. Kriewall, S. Karnati, M.C. Leu, J.W. Newkirk, Characterization of AISI 304L stainless steel powder recycled in the laser powder-bed fusion process, Addit. Manuf. 32 (2020) 100981. https://doi.org/10.1016/j.addma.2019.100981.
[20] F. Ahmed, U. Ali, D. Sarker, E. Marzbanrad, K. Choi, Y. Mahmoodkhani, E. Toyserkani, Study of powder recycling and its effect on printed parts during laser powder-bed fusion of 17-4 PH stainless steel, J. Mater. Process. Technol. (2019) 116522. https://doi.org/10.1016/j.jmatprotec.2019.116522.
[21] T. Delacroix, F. Lomello, F. Schuster, H. Maskrot, J.-P. Garandet, Influence of powder recycling on 316L stainless steel feedstocks and printed parts in laser powder bed fusion, Addit. Manuf. 50 (2022) 102553. https://doi.org/10.1016/j.addma.2021.102553.

[22] M. Hilzenthaler, L. Bifano, F. Scherm, G. Fischerauer, A. Seemann, U. Glatzel, Characterization of recycled AISI 904L superaustenitic steel powder and influence on selective laser melted parts, Powder Technol. 391 (2021) 57–68. https://doi.org/10.1016/j.powtec.2021.06.011.
[23] A.T. Sutton, C.S. Kriewall, S. Karnati, M.C. Leu, J.W. Newkirk, W. Everhart, B. Brown, Evolution of AISI 304L stainless steel part properties due to powder recycling in laser powder-bed fusion, Addit. Manuf. 36 (2020) 101439. https://doi.org/10.1016/j.addma.2020.101439.
[24] S.A. Khairallah, A.T. Anderson, A. Rubenchik, W.E. King, Laser powder-bed fusion additive manufacturing: Physics of complex melt flow and formation mechanisms of pores, spatter, and denudation zones, Acta Mater. 108 (2016) 36–45. https://doi.org/10.1016/j.actamat.2016.02.014.
[25] C.L.A. Leung, S. Marussi, R.C. Atwood, M. Towrie, P.J. Withers, P.D. Lee, In situ X-ray imaging of defect and molten pool dynamics in laser additive manufacturing, Nat. Commun. 9 (2018) 1355. https://doi.org/10.1038/s41467-018-03734-7.
[26] C.L.A. Leung, S. Marussi, M. Towrie, J. del Val Garcia, R.C. Atwood, A.J. Bodey, J.R. Jones, P.J. Withers, P.D. Lee, Laser-matter interactions in additive manufacturing of stainless steel SS316L and 13-93 bioactive glass revealed by in situ X-ray imaging, Addit. Manuf. 24 (2018) 647–657. https://doi.org/10.1016/j.addma.2018.08.025.
[27] Q. Guo, C. Zhao, L.I. Escano, Z. Young, L. Xiong, K. Fezzaa, W. Everhart, B. Brown, T. Sun, L. Chen, Transient dynamics of powder spattering in laser powder bed fusion additive manufacturing process revealed by in-situ high-speed high-energy x-ray imaging, Acta Mater. 151 (2018) 169–180. https://doi.org/10.1016/j.actamat.2018.03.036.
[28] P. Bidare, I. Bitharas, R.M. Ward, M.M. Attallah, A.J. Moore, Fluid and particle dynamics in laser powder bed fusion, Acta Mater. 142 (2018) 107–120. https://doi.org/10.1016/j.actamat.2017.09.051.
[29] T.-N. Le, Y.-L. Lo, K.-Y. Chen, W. Hung, Numerical and experimental investigation into powder entrainment and denudation phenomena in laser powder bed fusion process, Powder Technol. 410 (2022) 117907. https://doi.org/10.1016/j.powtec.2022.117907.
[30] M.J. Matthews, G. Guss, S.A. Khairallah, A.M. Rubenchik, P.J. Depond, W.E. King, Denudation of metal powder layers in laser powder bed fusion processes, Acta Mater. 114 (2016) 33–42. https://doi.org/10.1016/j.actamat.2016.05.017.
[31] S. Ly, A.M. Rubenchik, S.A. Khairallah, G. Guss, M.J. Matthews, Metal vapor micro-jet controls material redistribution in laser powder bed fusion additive manufacturing, Sci. Rep. 7 (2017) 1–12. https://doi.org/10.1038/s41598-017-04237-z.
[32] Y.A. Mayi, M. Dal, P. Peyre, M. Bellet, C. Metton, C. Moriconi, R. Fabbro, Laser-induced plume investigated by finite element modelling and scaling of particle entrainment in laser powder bed fusion, J. Phys. Appl. Phys. 53 (2019) 075306. https://doi.org/10.1088/1361-6463/ab5900.
[33] S. Traore, M. Schneider, I. Koutiri, F. Coste, R. Fabbro, C. Charpentier, P. Lefebvre, P. Peyre, Influence of gas atmosphere (Ar or He) on the laser powder bed fusion of a Ni-based alloy, J. Mater. Process. Technol. 288 (2021) 116851. https://doi.org/10.1016/j.jmatprotec.2020.116851.
[34] C. Pauzon, E. Hryha, P. Forêt, L. Nyborg, Effect of argon and nitrogen atmospheres on the properties of stainless steel 316 L parts produced by laser-powder bed fusion, Mater. Des. 179 (2019) 107873. https://doi.org/10.1016/j.matdes.2019.107873.
[35] C.L.A. Leung, S. Marussi, M. Towrie, R.C. Atwood, P.J. Withers, P.D. Lee, The effect of powder oxidation on defect formation in laser additive manufacturing, Acta Mater. 166 (2019) 294–305. https://doi.org/10.1016/j.actamat.2018.12.027.
[36] A. Masmoudi, R. Bolot, C. Coddet, Investigation of the laser-powder-atmosphere interaction zone during the selective laser melting process, J. Mater. Process. Technol. 225 (2015) 122–132. https://doi.org/10.1016/j.jmatprotec.2015.05.008.
[37] A. Ladewig, G. Schlick, M. Fisser, V. Schulze, U. Glatzel, Influence of the shielding gas flow on the removal of process by-products in the selective laser melting process, Addit. Manuf. 10 (2016) 1–9. https://doi.org/10.1016/j.addma.2016.01.004.

[38] M. Taheri Andani, R. Dehghani, M.R. Karamooz-Ravari, R. Mirzaeifar, J. Ni, A study on the effect of energy input on spatter particles creation during selective laser melting process, Addit. Manuf. 20 (2018) 33–43. https://doi.org/10.1016/j.addma.2017.12.009.
[39] M. Simonelli, C. Tuck, N.T. Aboulkhair, I. Maskery, I. Ashcroft, R.D. Wildman, R. Hague, A Study on the Laser Spatter and the Oxidation Reactions During Selective Laser Melting of 316L Stainless Steel, Al-Si10-Mg, and Ti-6Al-4V, Metall. Mater. Trans. A. 46 (2015) 3842–3851. https://doi.org/10.1007/s11661-015-2882-8.
[40] A.N.D. Gasper, B. Szost, X. Wang, D. Johns, S. Sharma, A.T. Clare, I.A. Ashcroft, Spatter and oxide formation in laser powder bed fusion of Inconel 718, Addit. Manuf. 24 (2018) 446–456. https://doi.org/10.1016/j.addma.2018.09.032.
[41] M. Lutter-Günther, M. Bröker, T. Mayer, S. Lizak, C. Seidel, G. Reinhart, Spatter formation during laser beam melting of AlSi10Mg and effects on powder quality, Procedia CIRP. 74 (2018) 33–38. https://doi.org/10.1016/j.procir.2018.08.008.
[42] A.T. Sutton, C.S. Kriewall, M.C. Leu, J.W. Newkirk, B. Brown, Characterization of laser spatter and condensate generated during the selective laser melting of 304L stainless steel powder, Addit. Manuf. 31 (2020) 100904. https://doi.org/10.1016/j.addma.2019.100904.
[43] C. Lu, R. Zhang, X. Wei, M. Xiao, Y. Yin, Y. Qu, H. Li, P. Liu, X. Qiu, T. Guo, An investigation on the oxidation behavior of spatters generated during the laser powder bed fusion of 316L stainless steel, Appl. Surf. Sci. 586 (2022) 152796. https://doi.org/10.1016/j.apsusc.2022.152796.
[44] A. Raza, C. Pauzon, E. Hryha, A. Markström, P. Forêt, Spatter oxidation during laser powder bed fusion of Alloy 718: Dependence on oxygen content in the process atmosphere, Addit. Manuf. 48 (2021) 102369. https://doi.org/10.1016/j.addma.2021.102369.
[45] C. Panwisawas, Y.T. Tang, R.C. Reed, Metal 3D printing as a disruptive technology for superalloys, Nat. Commun. 11 (2020). https://doi.org/10.1038/s41467-020-16188-7.
[46] P. Moghimian, T. Poirié, M. Habibnejad-Korayem, J.A. Zavala, J. Kroeger, F. Marion, F. Larouche, Metal powders in additive manufacturing: A review on reusability and recyclability of common titanium, nickel and aluminum alloys, Addit. Manuf. 43 (2021) 102017. https://doi.org/10.1016/j.addma.2021.102017.
[47] C. Kriewall, A. Sutton, S. Karnati, J. Newkirk, M.-C. Leu, Effects of Area Fraction and Part Spacing on Degradation of 304L Stainless Steel Powder in Selective Laser Melting, Proc. 28th Solid Free. Fabr. Symp. 2017 Austin TX. (2017) 277–288. https://scholarsmine.mst.edu/matsci_eng_facwork/2242.
[48] D. Galicki, F. List, S.S. Babu, A. Plotkowski, H.M. Meyer, R. Seals, C. Hayes, Localized Changes of Stainless Steel Powder Characteristics During Selective Laser Melting Additive Manufacturing, Metall. Mater. Trans. A. 50 (2019) 1582–1605. https://doi.org/10.1007/s11661-018-5072-7.
[49] H. Amano, Y. Yamaguchi, T. Ishimoto, T. Nakano, Reduction of Spatter Generation Using Atmospheric Gas in Laser Powder Bed Fusion of Ti–6Al–4V, Mater. Trans. 62 (2021) 1225–1230. https://doi.org/10.2320/matertrans.MT-M2021059.
[50] D. Wang, S. Wu, F. Fu, S. Mai, Y. Yang, Y. Liu, C. Song, Mechanisms and characteristics of spatter generation in SLM processing and its effect on the properties, Mater. Des. 117 (2017) 121–130. https://doi.org/10.1016/j.matdes.2016.12.060.
[51] R. Li, J. Liu, Y. Shi, L. Wang, W. Jiang, Balling behavior of stainless steel and nickel powder during selective laser melting process, Int. J. Adv. Manuf. Technol. 59 (2012) 1025–1035. https://doi.org/10.1007/s00170-011-3566-1.
[52] S.P. Lu, H. Fujii, K. Nogi, T. Sato, Effect of oxygen content in He–O2 shielding gas on weld shape in ultra deep penetration TIG, Sci. Technol. Weld. Join. 12 (2007) 689–695. https://doi.org/10.1179/174329307X238425.
[53] R. Yavari, Z. Smoqi, A. Riensche, B. Bevans, H. Kobir, H. Mendoza, H. Song, K. Cole, P. Rao, Part-scale thermal simulation of laser powder bed fusion using graph theory: Effect of thermal history on porosity, microstructure evolution, and recoater crash, Mater. Des. 204 (2021) 109685. https://doi.org/10.1016/j.matdes.2021.109685.

[54] R.L. Higginson, C.P. Jackson, E.L. Murrell, P.A.Z. Exworthy, R.J. Mortimer, D.R. Worrall, G.D. Wilcox, Effect of thermally grown oxides on colour development of stainless steel, Mater. High Temp. 32 (2015) 113–117. https://doi.org/10.1179/0960340914Z.00000000083.
[55] A.B. Anwar, I.H. Ibrahim, Q.-C. Pham, Spatter transport by inert gas flow in selective laser melting: A simulation study, Powder Technol. 352 (2019) 103–116. https://doi.org/10.1016/j.powtec.2019.04.044.
[56] C. Schwerz, A. Raza, X. Lei, L. Nyborg, E. Hryha, H. Wirdelius, In-situ detection of redeposited spatter and its influence on the formation of internal flaws in laser powder bed fusion, Addit. Manuf. 47 (2021) 102370. https://doi.org/10.1016/j.addma.2021.102370.